

# Magnetic Tweezers: Micromanipulation and Force Measurement at the Molecular Level

Charlie Gosse and Vincent Croquette

Laboratoire de Physique Statistique, École Normale Supérieure, Unité de Recherche 8550 associée au Centre National de la Recherche Scientifique et aux Universités Paris VI et VII, 75231 Paris, France

**ABSTRACT** Cantilevers and optical tweezers are widely used for micromanipulating cells or biomolecules for measuring their mechanical properties. However, they do not allow easy rotary motion and can sometimes damage the handled material. We present here a system of magnetic tweezers that overcomes those drawbacks while retaining most of the previous dynamometers properties. Electromagnets are coupled to a microscope-based particle tracking system through a digital feedback loop. Magnetic beads are first trapped in a potential well of stiffness  $\sim 10^{-7}$  N/m. Thus, they can be manipulated in three dimensions at a speed of  $\sim 10$   $\mu\text{m/s}$  and rotated along the optical axis at a frequency of 10 Hz. In addition, our apparatus can work as a dynamometer relying on either usual calibration against the viscous drag or complete calibration using Brownian fluctuations. By stretching a DNA molecule between a magnetic particle and a glass surface, we applied and measured vertical forces ranging from 50 fN to 20 pN. Similarly, nearly horizontal forces up to 5 pN were obtained. From those experiments, we conclude that magnetic tweezers represent a low-cost and biocompatible setup that could become a suitable alternative to the other available micromanipulators.

## LIST OF SYMBOLS

$A_u$	( $\text{NA}^{-1}$ ) the factor between the force and the current flowing in the coils (Defined in Eq. 2)	$\Gamma_{x,y}$	(nondimensional) the viscous coefficient of a sphere moving parallel to a sidewall (Defined in Eq. 30)
$\alpha$	(nondimensional) the proportional feedback factor in the digital model (Defined in Eq. 11)	$\Gamma_z$	(nondimensional) the viscous coefficient of a sphere moving perpendicularly to a sidewall (Defined in Eq. 30)
$B_u$	( $\mu\text{m s}^{-1}\text{A}^{-1}$ ) the proportional factor between the velocity of a bead and the associated driving current (Defined in Eq. 19)	$I_u$	(A) the coil driving current (Defined in Eq. 1)
$\beta$	(nondimensional) the ratio between the integral and the proportional feedback factors (Defined in Eq. 17)	$I_{\text{um}}$	(A) the maximum current set in one direction (Defined in Characterization of the Active Tweezers).
$C_u$	(nondimensional) the correction signal in feedback loop (Defined in Eq. 1)	$I_0$	(A) the minimal value of $I_z$ that lift the magnetic particle. (Defined in Design of the Apparatus).
$Cr(f)$	(nondimensional) the camera filtering correction due to its finite integration time (Defined in Eq. 32)	$k_u$	( $\text{Nm}^{-1}$ ) the stiffness of the tweezers (Defined in Eq. 2)
$D$	( $\mu\text{m}^2\text{s}^{-1}$ ) the bead diffusion coefficient (Defined in Eq. 9)	$K_u$	( $\mu\text{m}^{-1}$ ) the integral coefficient in the feedback loop (Defined in Eq. 1)
$\delta t$	(s) the time interval between two video frames (40 ms) (Defined in Eq. 12)	$L_0^2(f)$	( $\mu\text{m}^2\text{Hz}^{-1}$ ) the Langevin force noise density in Fourier space (Defined in Eq. 14)
$\delta t_i$	(s) the time integration of the video camera ( $0.97 \delta t$ ) (Defined in Eq. 32)	$P_u$	( $\mu\text{m}^{-1}$ ) the proportional coefficient in the feedback loop (Defined in Eq. 1)
$\Delta$	(nondimensional) the delay in the feedback loop (Defined in Eq. 11)	$r$	( $\mu\text{m}$ ) the bead radius (Defined in Eq. 7)
$\Delta T$	(s) the integration time of the signal (Defined after Eq. 10)	$V_u$	( $\mu\text{m s}^{-1}$ ) the bead velocity (Defined in Eq. 9)
$\eta$	(poise) the fluid viscosity (Defined in Eq. 7)		
$F_u$	(N) the force acting on the bead (Defined in Eq. 2)		
$F_L$	(N) the random Langevin force responsible for the Brownian motion (Defined in Eq. 7)		
$f_c$	(Hz) the cutoff frequency of the bead attached to the molecule system, $f_c = k_u/(2\pi\Gamma\eta r)$ (Defined in the paragraph just after Eq. 8).		
$f_s$	(Hz) the sampling frequency of the camera (25 Hz here), $f_s = 1/\delta t$ (Defined in Eq. 31)		
$f_L$	(Hz) the smallest usable frequency, $f_L = 1/\Delta T$ (Defined after Eq. 10)		
$\Gamma$	(nondimensional) the viscous coefficient of a sphere, usually $6\pi$ (Defined in Eq. 7)		

## INTRODUCTION

During the last ten years, single biomolecule micromanipulations have revolutionized the field of biophysics (Bensimon, 1996; Bustamante et al., 2000), allowing the biophysicists 1) to measure the elastic behavior of biopolymers such

Submitted July 6, 2001, and accepted for publication February 21, 2002.

Dr. Gosse's present address is Institut Curie, Paris, France. E-mail: charlie.gosse@curie.fr.

Address reprint requests to Vincent Croquette, Laboratoire de Physique Statistique, École Normale Supérieure, 24 rue Lhomond, 75231 Paris, France. Tel.: +33-1-44-32-34-92; Fax: +33-1-44-32-34-33; E-mail: vincent@physique.ens.fr.

© 2002 by the Biophysical Society

0006-3495/02/06/3314/16 \$2.00

as actin (Kishino and Yanagida, 1988), titin (Kellermayer et al., 1997; Carrion-Vazquez et al., 1999), or DNA (Cluzel et al., 1996; Strick et al., 1996); 2) to determine the tensile strength of single ligand/receptor bond (Florin et al., 1994; Merkel et al., 1999); 3) to investigate the micromechanics of molecular motors such as kinesin (Block et al., 1990) and myosin (Ishijima et al., 1991; Finer et al., 1994); 4) to follow in real time the activity of single proteins such as polymerases (Yin et al., 1995; Maier et al., 2000; Wuite et al., 2000b); and even 5) to observe single enzymatic cycles of individual enzymes (Noji et al., 1997; Strick et al., 2000).

Micromanipulation implies monitoring of forces at the molecular scale. In biology, at the single-molecule level, the characteristic energy is given by the hydrolysis of ATP (20  $kT$  i.e., 80 pN·nm) and the characteristic size by the diameter of a protein (a few nanometers). The resulting forces that biophysicists must be able to measure and to produce while studying those objects are therefore in the range of hundreds of femtonewtons to tens of piconewtons. In most of the previously mentioned studies, the biomolecule is attached to a micromanipulator that works like the spring of a dynamometer: after measuring the stiffness of the spring, forces are deduced from extension measurements. Examples of micromanipulators include atomic force microscopy cantilevers (Moy et al., 1994; Carrion-Vazquez et al., 1999), glass fibers (Kishino and Yanagida, 1988; Cluzel et al., 1996), biomembrane force probes (Evans and Ritchie, 1997; Merkel et al., 1999), and microbeads held by optical tweezers (Block et al., 1990; Finer et al., 1994; Wuite et al., 2000a). Typical stiffness ranges from 1 N/m for the former to  $10^{-5}$  N/m for the latter. For measuring biological forces, the typical extensions that must be detected are consequently of a few nanometers; a distance also characteristic of the step-size of molecular motors (Schnitzer and Block, 1997). In this article, we report a new kind of micromanipulator in which micrometric particles are monitored and manipulated in three dimensions (3D) using magnetic field gradients and servo loops. Our apparatus fulfills all the single molecule biophysics requirements previously mentioned and presents an alternative to the various existing dynamometers and manipulators.

The early setups able to manipulate magnetic objects in solution were constructed by biophysicists for the *in vivo* study of the viscoelastic properties of the cytoplasm (Crick and Hughes, 1949; Yagi, 1960). More recently, this technique has been applied to the rheology of actin filament solutions. After the first experiments by Sackmann and co-workers (Ziemann et al., 1994), in which the motion of magnetic particles was confined to a single horizontal axis, Amblard et al. (1996a,b) built a micromanipulator for precise and easily controlled two-dimensional translation and rotation of micrometric beads. Independently, magnetic piconewton-force transducers have been used to investigate the elastic behavior of phospholipidic membranes (Heinrich and Waugh, 1996; Simson et al., 1998). Forces ranging

from hundreds of femtonewtons to nanonewtons were measured, but micromanipulation of the particle was not possible. A somewhat similar apparatus was recently described (Haber and Witz, 2000) with a special care to obtain a uniform force on a large spatial domain (1.5 cm). Very accurate positioning and force measurements have also been demonstrated using a macroscopic magnetic particle levitated by a single coil (Gauthier-Manuel and Garnier, 1997). Pursuing those works, we report here the design of a magnetic micromanipulator that could also be used as a new tool for scientific exploration at the single-biomolecule level.

In its application, our apparatus is very similar to optical tweezers (Svoboda and Block, 1994; Simmons et al., 1996), it allows displacement of small beads (a few microns in diameter) in solution and to use them as handles or picodynamometers. The positioning of the particle in 3D is achieved with a precision of a few nanometers and forces from a few tenths to tens of piconewtons are simultaneously measured. In the optical tweezers experiment, a particle having a larger refractive index than its surrounding medium is trapped by the radiation pressure of a focused laser beam. The intensity profile of the beam corresponds to a real potential well that traps the bead in a precise location. In our setup, a system of electromagnets creates field gradients, producing a force on a super-paramagnetic object. Adjusting the current running through the coils allows us to change the intensity and the direction of this force. Furthermore, by combining, in a feedback loop, this manipulator with a video-positioning system, we are able to control the 3D position of the particle in real time. Note that, in this case, the action of the magnets is global and the particle is, in fact, trapped in a virtual potential well by the servo loop. Additionally, we may rotate the object while holding it fixed because the direction of the field imposes the angular orientation of the particle magnetic dipole. Finally, after calibration of the apparatus, the force acting on the particle can be determined by measuring the currents driving the electromagnets.

The magnetic tweezers described here share most of the features of optical tweezers while offering the advantage of angular positioning. Moreover, this apparatus does not require a laser that might photodamage the biomaterial (Liu et al., 1996; Neuman et al., 1999). We believe that it could, in the future, meet cell biologists' needs and allow them precise positioning of organelles, *in vivo* microrheological investigations (Crick and Hughes, 1949; Yagi, 1960), and force measurements (Wang et al., 1993; Guilford et al., 1995).

## DESIGN OF THE APPARATUS

### Principle

The apparatus consists of two distinct parts: a 3D positioning algorithm (discussed later in this section) and a set of electromagnets allowing the 3D displacement of the studied particle (discussed in the next subsection).

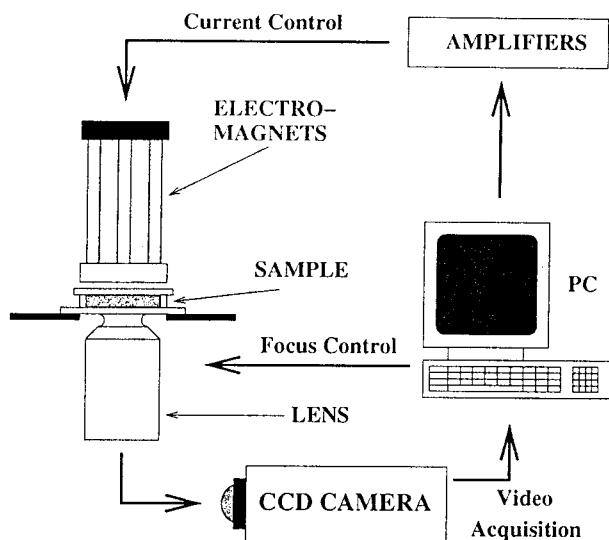


FIGURE 1 General magnetic tweezers setup. A thin sample is observed with an inverted microscope, a CCD image is processed by a computer that drives the electromagnets to servo the bead position in real time.

As described in Fig. 1, the cell containing the magnetic particles in solution is held on the stage of an inverted microscope. This cell is typically a small capillary tube with a rectangular section (thickness of  $300\ \mu\text{m}$ ; Vitrocom, Mountains Lakes, NJ). Its top and bottom surfaces are of good optical quality. A system of six vertical electromagnets with their pole pieces arranged in a hexagonal pattern is placed just above the capillary tube. Parallel light illuminates the sample through a 2-mm-diameter aperture located at the center of the hexagon. An  $xyz$  translation stage allows the accurate positioning of the electromagnets with respect to the optical axis of the objective.

During micromanipulation, a magnetic particle is located with nanometer accuracy by video analysis. The computer program determines its position in the three spatial dimensions at video rate. Then the digital feedback loop adjusts the current in each electromagnet to cancel the difference between the desired and the observed positions of this bead. The six-fold symmetry of the electromagnets allows rotation of the direction of the magnetic field and hence of the magnetic particle itself. The force applied to the bead can be directly evaluated by Brownian motion analysis (Strick et al., 1996; Allemand, 1997). This method allows the detection of forces ranging from tens of femtonewtons to tens of piconewtons. Alternatively, the force can be read from the currents driving the coils. This requires previous force calibration against the viscous drag or against the Brownian fluctuations.

The present apparatus is inspired from our previous setup using permanent magnets where position and angle were controlled through simple motorized stages (Strick et al., 1998), allowing stretching and twisting of DNA molecules.

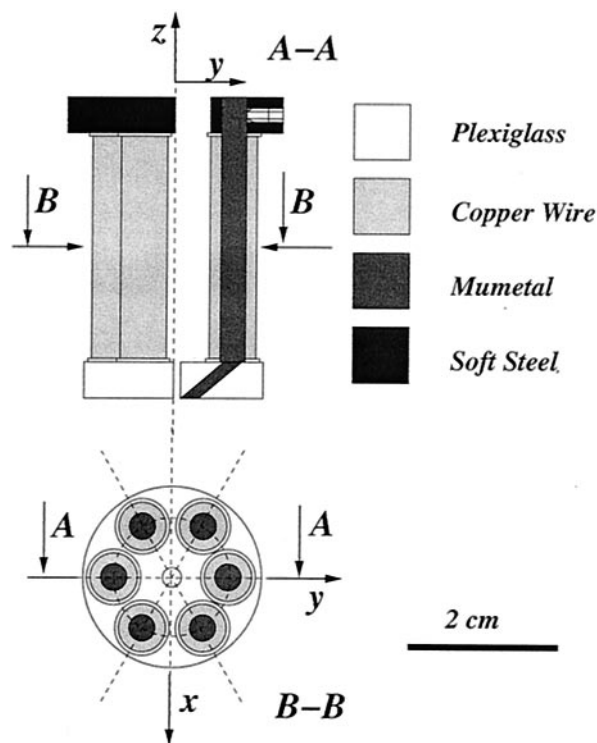


FIGURE 2 Detailed mechanical setup of the electromagnets. The six coils are placed in a hexagonal geometry, the magnetic field gradients occur between the tips of the mumetal pole pieces. With this configuration, the magnitude and direction of the force acting on the bead can be altered by modulating the driving currents in the coils.

The electromagnets allow faster control, which is necessary for operation in a tweezers mode.

## Magnetic field

### Coils and pole pieces

The six vertical coils (Fig. 2) are attached to a soft steel base and are capped by curved pole pieces. The soft steel ring is designed to close the field lines in the system, thus increasing the magnitude of the magnetic field. A cylinder of Plexiglas fixed at the pole-pieces end improves the mechanical cohesion of the apparatus.

The round piece closing the field lines is made of XC15 soft steel (Tonnetot Metaux, Fontenay-sous-Bois, France) and the pole pieces are cylinders of mumetal (Goodfellow, Cambridge, U.K.). Those two alloys were chosen for their low remanent magnetization (20 gauss for mumetal). Coils (Lima 600880, Vizenza, Italy) are made of copper wire and have a resistance of  $10 \pm 0.2\ \Omega$ . Each of them is driven by a current-power amplifier connected to the computer by a digital-to-analog converter. To avoid magnetic hysteresis, each change of the coil-driving current is accomplished with an exponentially decaying oscillating component added (the amplitude being the change size divided by two at each

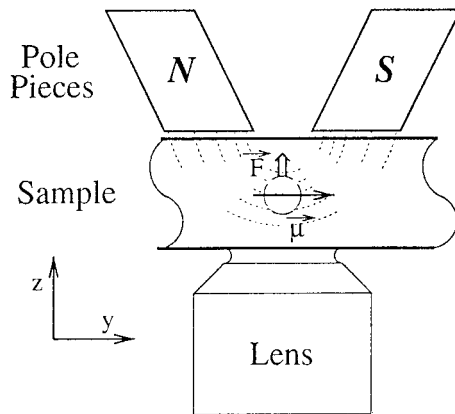


FIGURE 3 Coils and pole pieces produce a horizontal magnetic field in the middle of the sample. The magnetic moment  $\vec{\mu}$  of the bead aligns with the field lines and the vertical magnetic field gradient exerts a force  $\vec{F}$  that raises the super-paramagnetic object.

period, i.e., every 4 ms). With low hysteresis materials, this method assigns a unique value of the magnetic field to the driving current. A more sophisticated method has been used in other experiments (Amblard et al., 1996b), where an active control of the magnetic field through Hall probes fixed at the end of each pole piece feed back the current in the associated coil.

#### Current configurations and bead movement

The coils have been designed to produce on the bead a force whose three components may be adjusted independently. Furthermore, various experimental constraints had to be overcome: the microscope objective and the light illumination path did not allow placement of coils along the vertical optical axis; some symmetry had to insure the rotation ability. We have found that a set of six vertical electromagnets placed in hexagonal pattern over the sample was adequate. However, the present system can only apply a force directed upward; the downward motion of the bead relies upon gravity. This is certainly a limitation in this apparatus, but it can be overcome in the future by a more complex set of electromagnets. The six coils used here represent a minimal system that, for the sake of simplicity, will be discussed in this paper.

We will first describe how a force is generated in the  $z$  direction and then along the  $x$  and  $y$  axis. Let us assume that the six coils are numbered clockwise from 0 to 5 with coils 1 and 4 laying along the  $y$  axis. To produce a vertical force, we generate a horizontal magnetic field collinear to  $y$  and varying strongly along  $z$  (Fig. 3). If the three coils 0, 1, and 2 are run by a current  $I_z$  and the three opposite ones 3, 4, and 5 by a current  $-I_z$  (Fig. 4 A), a vertical force will be applied on every bead located close to the center of the hexagon. This force can easily overcome the weight of each particle and lift it. Beads are then simply returned to the ground by

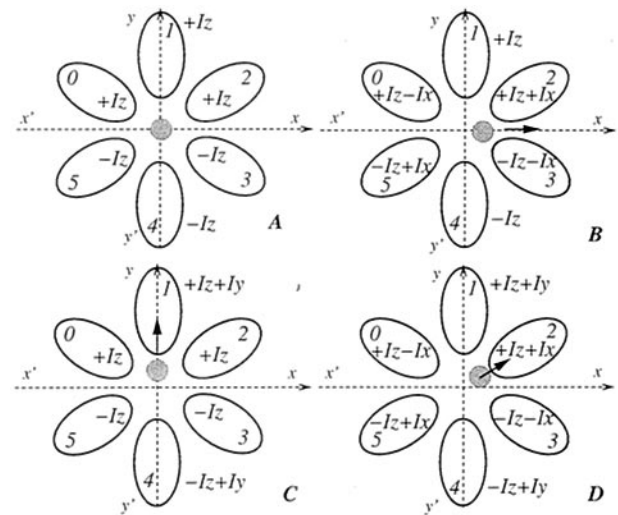


FIGURE 4 Schematic representation of the principles governing the bead displacement (top view of the sample). (A, B, and C) Three different current configurations are used to move the magnetic particle along  $z$ ,  $x$ , and  $y$ . (D) More complicated displacements can be reached by linear combination of the basic settings. Note that, in this figure, all the currents ( $I_x$ ,  $I_y$ , and  $I_z$ ) are positive.

reducing the currents: they fall under the effect of the gravity. A feedback loop adjusting  $I_z$  can finally stabilize the vertical position of a selected bead. However, the levitated particle will rapidly diffuse in  $x$  and  $y$ .

Now, suppose that the mean value of the current  $I_z$  creates a force that exactly equilibrates the effects of gravity (Fig. 4 A). If an excess current  $I_x$  runs in coils 2 and 3 while coils 0 and 5 have their driving current reduced by the same amount (Fig. 4 B), the  $x$  axis symmetry is broken and a horizontal field gradient is generated: the bead moves along the  $x$  axis toward the coils producing the strongest fields. Comparing the  $I_x$  and  $-I_x$  configurations, it is clear that the vertical force is the same, whereas the horizontal one changes its sign. If this  $I_x$  is not too large, the horizontal force acting on the particle is then proportional to  $I_x$  while, for symmetry reason, the vertical component of the magnetic force has zero linear dependence and is only affected to the second order.

Motion along the  $y$  axis may be obtained from the initial configuration by adding a current  $I_y$  in the two coils 1 and 4, so that  $I_z + I_y$  flows in 1 and  $-I_z + I_y$  in 4. The magnetic field is then reinforced around coil 1 and reduced around coil 4: as a result the particle moves toward the strongest electromagnet (Fig. 4 C). Again, the horizontal component of the force is proportional to  $I_y$  while the vertical one varies only quadratically with this additional current.

The sensitivity factor between the two axes differs, the symmetry breaking in  $x$  being stronger than in  $y$ . Oblique displacement of the bead (Fig. 4 D) may also be obtained through a linear combination of the two previous perturbations  $I_x$  and  $I_y$  (Table 1)

**TABLE 1** Current settings used to drive the electromagnets in the normal and the altered configurations\*

Coil Number	Normal Configuration	Altered Configuration	
		$I_x > I_z$	$I_x < -I_z$
0	$I_z - I_x$	0	$2I_z$
1	$I_z + I_y$	$2I_z - I_x$	$2I_z + I_x$
2	$I_z + I_x$	$2I_z$	0
3	$-(I_z + I_x)$	$-2I_z$	0
4	$-I_z + I_y$	$-2I_z + I_x$	$-2I_z - I_x$
5	$-(I_z - I_x)$	0	$-2I_z$

\*The altered configuration is used when  $|I_x| > I_z$ . The resulting force direction is presented in Fig. 7.

Despite  $I_z$  being only positive, for each bead one finds a characteristic current  $I_0$  above which the bead rises and below which it falls. Both  $I_x$  and  $I_y$  may be positive or negative, but, as detailed below, their absolute values had been set proportional to  $I_z$ . Finally, it is worth noting that nearly horizontal force can be applied along  $x$  by altering the current configuration as described in Table 1.

## Video acquisition and data treatment

Images of the sample are collected through the  $100\times$  oil immersion objective of an inverted microscope (Leica DMIRBE). A CCD camera (Sony XC-77CE) operating in 50-Hz field mode sends the data to a video acquisition card (ICPCI, Imaging Tech., Bedford, MA) installed in a computer.

Three-dimensional tracking of the bead is achieved in real time by a computer program. Typically, we analyze 25 images per second but twice this acquisition speed could even be reached by alternately using even and odd video frames. Evaluation of the particle displacement from one field to the next is done with sub-pixel resolution for time lapses of a few seconds (Allemand, 1997). At longer time scales, the experimental noise has a  $1/f$  component that decreases the precision. The  $x$ ,  $y$  positions are first obtained by real-time correlation of the bead images (Gelles et al., 1988). Then the  $z$  position is obtained by using parallel illumination: the bead image is surrounded with diffraction rings the diameter of which increases with the distance of the particle from the focal plane. The  $x$ ,  $y$  position is measured with an accuracy of a few nanometers whereas  $z$  is determined with a 10-nm resolution (see Appendix for more details).

## Digital feedback loop

Digital proportional-integral feedback loops are used to lock a particle in a given position. In the horizontal plane, the

currents  $I_x$  and  $I_y$  are chosen to be proportional to the main current  $I_z$  and are calculated as

$$I_u = -I_z C_u \quad \text{with} \quad C_u = [P_u \cdot u + K_u \sum (u)]. \quad (1)$$

In this equation,  $u$  corresponds to the error signal between the present position of the particle and the set one;  $P_u$  and  $K_u$  are, respectively, the proportional and integral coefficients,  $\sum (u)$  is the sum over the previous error signals; and  $C_u$  is the normalized correction signal.

Using only a proportional correction is equivalent to generating a force proportional to  $u$ , i.e., attaching the bead to a virtual spring whose stiffness  $k_u$  is directly determined by  $P_u$ . Writing  $A_u$ , the proportionality factor between the force and the driving current associated with direction  $u$ ,  $F_u = A_u \cdot I_u$ , we have

$$F_u = -A_u I_z P_u \cdot u \quad \text{and} \quad k_u = A_u I_z P_u. \quad (2)$$

Adding an integral term ( $K_u \sum (u)$ ) is important to stabilize the bead to its exact reference position in the presence of a constant and continuously applied force (e.g., gravity). In this case, Eq. 2 becomes

$$F_u = -A_u I_z C_u. \quad (3)$$

The feedback in the  $z$  direction is done by monitoring  $I_z$ . However, the force applied on the bead is not a linear function of this current. In the low force regime ( $F_z < 1$  pN), the magnetic field does not saturate the bead magnetization and thus  $F_z$  varies like  $I_z^2$  ( $F_z = A_z I_z^2$ ; see below, next section). To insure a correct feedback, we then apply a square-root function to the error signal,

$$I_z = I_0 \sqrt{-(P_z \cdot z + K_z \sum (z))}, \quad (4)$$

with  $I_0$  being the current just required to equilibrate the bead weight.

When the forces applied to the bead are small, the previous relations can be linearized around their means values,

$$I_z = I_0 \left( 1 - \frac{P_z \cdot z}{2} \right) \quad (5)$$

and

$$F_z = mg - A_z I_0^2 P_z \cdot z.$$

Thus, the tweezers vertical stiffness is given by

$$k_z = A_z I_0^2 P_z. \quad (6)$$

## CHARACTERIZATION OF THE PASSIVE TWEEZERS

Before describing the tweezers mode, let us discuss the forces generated by the electromagnets. They may be conveniently characterized by suppressing the feedback loop while maintaining the bead in position by tethering it with a

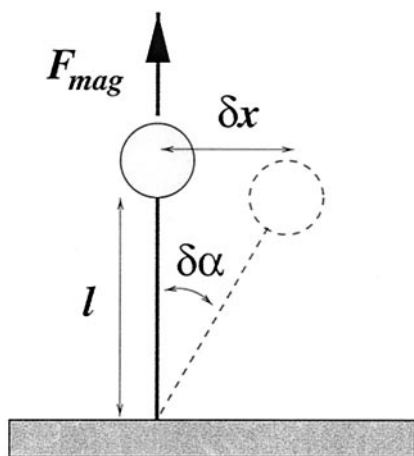


FIGURE 5 Principle of force measurement. The vertical magnetic force  $F_{mag}$  applied to the bead stretches the DNA molecule. The transverse Brownian fluctuations  $\langle \delta x^2 \rangle$  of this inverted pendulum are then used to evaluate its rigidity  $F_{mag}/l$  and thus the pulling force  $F_{mag}$ .

DNA molecule. Indeed, this method allows application of strong forces in any direction.

We have prepared both  $\lambda$  and pX $\Delta$ II DNA molecules (resp.  $\sim 16$  and  $5 \mu\text{m}$  long) with one extremity labeled with digoxigenin and the other with biotin. Incubating these molecules with streptavidin-coated super-paramagnetic beads  $4.5 \mu\text{m}$  in diameter (Dynabeads, Dynal, Oslo, Norway) results in the attachment of the particle to the biotin end of the biopolymer. Injection of these beads into an antidigoxigenin-coated glass capillary allows the dioxigenin end of the DNA to attach to the tube surface.

### Force measurements along z

We have first used the electromagnets configuration, which produces a force only along the  $z$  axis (Fig. 4 A). In this situation, the bead behaves as an inverted pendulum immersed in a thermal bath at temperature  $T$ . As we have shown in our previous work (Strick et al., 1996), the analysis of the horizontal Brownian motion of the particle permits measurement of the stretching force. More precisely, the bead-positioning software determines the DNA extension  $l$  and the particle transverse fluctuations  $\delta x$ . Using the equipartition theorem, the vertical magnetic force  $F_{mag}$  may then be evaluated through the simple formula,  $F_{mag} = k_B T l / \langle \delta x^2 \rangle$  (Fig. 5).

By ramping the current in the coils, we could construct the force versus extension curve of the DNA molecule (Fig. 6 A). The tweezers develop a force along  $z$  varying from 50 fN to 20 pN. Below 1 pN, we found the expected  $F_z \propto I_z^2$  behavior characteristic of unsaturated magnetic materials (Fig. 6 B); then, around 20 pN, saturation occurred. This maximum force is only five times smaller than the one we were able to apply using permanent magnets (Allemand et

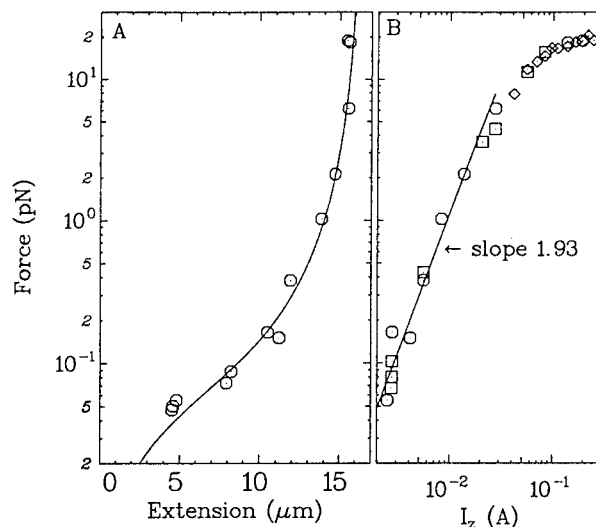


FIGURE 6 (A) Force versus extension curve measured for a  $4.5\text{-}\mu\text{m}$  bead attached to a  $\lambda$  DNA molecule. The full line is a fit to the worm-like chain model with a persistence length of 50 nm. (B) The current  $I_z$  producing the corresponding vertical force  $F_z$ . Data were collected with different DNA molecules.

al., 1998). Higher forces could certainly be produced by using magnetic materials with higher saturation field.

### Modulation of the force direction

Taking advantage of the DNA nonlinear elasticity described by the worm-like chain model (Bouchiat et al., 1999), we investigated the ability of the tweezers to pull particles in an arbitrary direction. Indeed, for stretching forces larger than 1 pN, the length of the dsDNA molecule varies little and the position of the bead relative to the biopolymer-anchoring point indicates the force direction.

As may be seen in Fig. 7, the stretching-force direction sweeps a very large angle in the  $x$  direction while keeping a modulus  $\approx 5$  pN as determined by Brownian motion analysis. The pulling angle reaches  $\pm 70^\circ$  at high stretching force where the weight of the bead is negligible ( $F > 1$  pN). In the  $y$  direction, similar results are obtained, but the pulling angle only reaches  $\pm 50^\circ$ . At lower forces, the weight of the bead combines with the magnetic force and allows the resulting force to point in all spatial directions. Pulling a DNA molecule nearly horizontally could be useful, for instance, to visualize enzymes moving along this polymer.

### CHARACTERIZATION OF THE ACTIVE TWEEZERS

Ideal tweezers should allow manipulation of a micrometric bead while giving access to the three force components at the same time. This is nearly achieved in the present setup

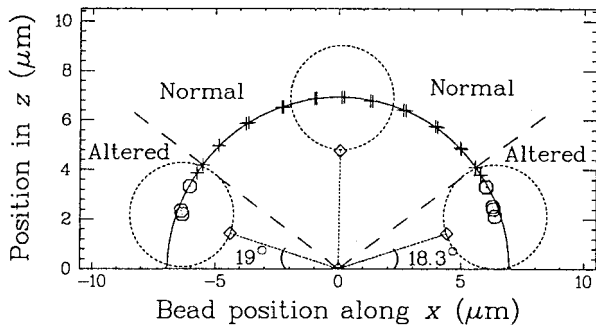


FIGURE 7 Positions of the bead center for the full range of  $x$  current modulation. The particle,  $4.5 \mu\text{m}$  in diameter, is tethered to the glass surface by a pX $\Delta$ II DNA molecule  $\sim 5 \mu\text{m}$  long. The position of the bead and of the DNA molecule are drawn in vertical position and for the maximum modulations. The circle is a fit to the data points obtained for moderate modulation (+). These points are typically within 20 nm away from the circle, demonstrating that the pulling force is unchanged. In the extreme modulations (O) the pulling direction is nearly horizontal and is limited by the fact that the bead touches the glass surface. For those extreme modulations, the stretching force decreases slightly as indicated by the shorter extension. The two long dashed lines indicate the boundary between the normal and the altered configuration of the coil-driving currents (see Table 1).

by recording the electromagnets driving currents. Nevertheless, it is of course necessary to previously perform tweezers calibration, i.e., to investigate the relation between currents and forces. In the small-force regime, these relations are linear, and thus the calibration consists of measuring the different proportionality constants  $A_u$ . These coefficients vary from one magnetic bead to another. However, we will show below that such a calibration can be achieved easily by recording the particle fluctuations in the trapped state with no external force applied.

To explain the tweezers properties and the related calibration procedure, we first introduce a simplified model with only an instantaneous proportional feedback. This model depends only on two parameters: the tweezers elastic stiffness  $k_u$  and the particle viscous drag coefficient  $\Gamma\eta r$ . We show that the analysis of the bead fluctuations in Fourier space allows determination of  $\Gamma\eta r$  at high frequencies and  $k_u$  at low frequencies. The measurement of  $\Gamma\eta r$  leads to the viscosity of the fluid  $\eta$ , and the measurement of  $k_u$  leads to the  $A_u$  through Eq. 2. Consequently, the tweezers may be used in two different operating modes: as a viscosimeter or as a dynamometer.

Finally, we discuss the properties of the real apparatus with its slower digital feedback and its integral correction. In this case, the tweezers cannot be described anymore by our simplified model, but are better characterized by a recursive equation accounting for the servo loop delay. Within this new context, we present three complementary calibration methods that provide absolute measurements of the force. Because the techniques and models used here are sometimes similar to the ones used for optical tweezers

calibration, the following analysis can be read in parallel with the reviews, Svoboda and Block (1994), and Gittes and Schmidt (1998).

### Model for ideal tweezers

To study the complete feedback loop of our apparatus, a  $4.5\text{-}\mu\text{m}$  super-paramagnetic bead is locked  $10 \mu\text{m}$  above the surface. As seen above, couplings among the  $x$ ,  $y$ , and  $z$  forces are only quadratic, and, consequently, the three trapping directions may be considered as independent. For the sake of simplicity, we will also first work with a proportional feedback. Furthermore, we will assume that the feedback presents no delay, which allows a simple description of “ideal” tweezers. The bead is locked in a virtual one-dimensional potential well where the magnetic tweezers respond with a force  $F_u = -k_u \cdot u$  to a deviation  $u$  from the initial set position. The equation of motion of the particle can thereby be written,

$$m \frac{d^2u}{dt} + \Gamma\eta r \frac{du}{dt} + k_u u = F_L, \quad (7)$$

where  $m$  is the mass of the bead,  $r$  its radius,  $\eta$  the viscosity of the solution, and  $\Gamma$  the viscous drag coefficient ( $6\pi$  for a spherical object far from any surface). It is easy to verify that the system is overdamped and the inertial term may thus be omitted.  $F_L$  is the stochastic Langevin force responsible for the fluctuations characteristic of the Brownian motion of the particle. From the fluctuation dissipation theorem, it follows that  $\langle F_L(t) \rangle = 0$  and  $\langle F_L(t)F_L(t') \rangle = 2k_B T \Gamma\eta r \delta(t - t')$ , which appears as a white noise in Fourier space,  $|F_L(f)|^2 = 4k_B T \Gamma\eta r$ . Note that this noise is also the intrinsic noise of our measurement.

In frequency space, the density of fluctuations is then given by

$$|u(f)|^2 = \frac{4k_B T \Gamma\eta r}{|k_u + i\Gamma\eta r 2\pi f|^2} = 4k_B T \frac{\Gamma\eta r}{k_u^2} \frac{1}{1 + (f/f_c)^2}, \quad (8)$$

where  $f_c = k_u/(2\pi\Gamma\eta r)$ . This power spectrum is a Lorentzian corresponding to the response function of a bead attached to a spring, immersed in a viscous medium, and excited by a white noise (the Langevin force). This noise depends only on dissipative terms, it is proportional to  $\eta$  and  $r$ . More precisely, at low frequencies ( $f \ll f_c$ ), the power spectrum presents an asymptotic white noise determined by the excitation of the spring  $k_u$  through the Langevin noise, whereas, at high frequencies ( $f \gg f_c$ ), the  $f^{-2}$  behavior is dominated by the viscous term  $\Gamma\eta r$  (Fig. 8 at small  $P_z$  values).

#### Viscosimeter mode

Because, at high frequencies, the Brownian fluctuations of the bead presents a  $1/f^2$  regime (see Fig. 8), the spectrum of

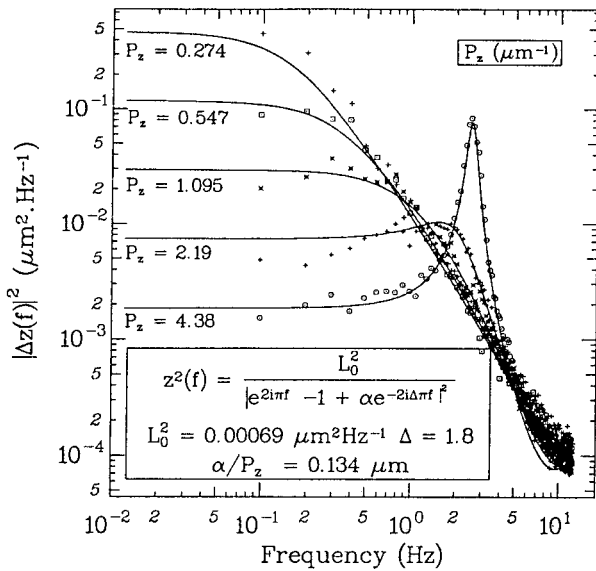


FIGURE 8 *Data points.* Average power spectra of the vertical position fluctuations of a trapped bead (only a variable proportional feedback is applied here). These power spectra have a Lorentzian shape when the feedback is small (*top curves*). As the feedback is increased, the fluctuations decrease and the cutoff frequency increases. At high feedback, ringing occurs (*bottom curves*). *Solid lines.* Power spectra obtained from the iterative model.  $L_0^2$ ,  $\alpha$ , and  $\Delta$  were first determined by fitting the lowest power spectrum to Eq. 16 ( $\Delta$  can only be evaluated when ringing occurs, i.e. at high  $P_z$ ). The other spectra were then fitted while keeping  $L_0^2$  and  $\Delta$  equal to the found values. Finally, the proportionality between  $\alpha$  and  $P_z$  ( $\alpha = A_z I_0^2 P_z \delta t / \Gamma \eta r$  [Eqs. 6 and 13]) was checked.

the velocity fluctuations (the derivative  $V_u$ ) presents an asymptotic white noise, the value of which is proportional to the object diffusion coefficient  $D$  and thus inversely proportional to the viscous term  $\Gamma \eta r$ ,

$$V_u^2(f \gg f_c) = \frac{4k_B T}{\Gamma \eta r} = 4D. \quad (9)$$

Consequently, the particle Brownian motion offers a simple means to use the magnetic tweezers as a viscosimeter *in vitro* (Ziemann et al., 1994; Amblard et al., 1996b) or *in vivo* (Crick and Hughes, 1949; Sato et al., 1984; Zaner and Valberg, 1989; Yagi, 1960). First, the tweezers bring a bead to a specific point of interest. Then, the feedback is switched to a low-stiffness mode, which allows measurement of the local viscosity while keeping the probe in a defined area. Accurate data may be obtained at such low-feedback parameters because the cutoff frequency is small, leaving a wide white-noise regime in the bead-velocity spectrum. Additionally, care must be taken to compensate for the video camera filtering due to exposure-integration damping of the frequencies close to the acquisition rate.

#### Tweezers mode

The measure of  $k_u$  leads to the calibration of the apparatus as a dynamometer. When the tweezers can be considered as ideal,

the calibration procedure can be achieved by using the equipartition theorem. Provided that we record the bead fluctuations with an infinite frequency range, we can write  $k_B T/2 = k_u \langle u^2 \rangle / 2$  in real space. Thus, in Fourier space, we have

$$k_u = \frac{k_B T}{\int_0^\infty df |u(f)|^2}. \quad (10)$$

This calibration method is very powerful, but, as explained below, it applies to the magnetic tweezers only when the values of the feedback parameters are low (i.e., when the  $P_u$  are small). We will first discuss here the intrinsic limitations of the method and its validity conditions. Then, we will show that, although this method cannot be used directly when the values of the feedback parameters are high, it may be adapted to this situation.

The two intrinsic limitations of the equipartition calibration are finite bandwidth and accuracy. In all experiments, the signal bandwidth is limited at high frequency to the half of the sampling rate  $f_s/2$  and at low frequency to the inverse of the observation window  $f_L = \Delta T^{-1}$ . Thus, the integration limits in Eq. 10 becomes  $f_L$  and  $f_s/2$  instead of 0 and  $\infty$ . To maintain the accuracy of this relation, we must either ensure that  $f_s/2 \gg f_c \gg f_L$  or correct the equation from the limited integration range. This last method requires evaluation of the integral of the Lorentzian within the experimental range to determine  $f_c$ .

Independently, it is worth noting that the estimation of  $f_c$  is also useful to evaluate the statistical error on  $\langle u^2 \rangle$  and thus on  $k_u$ . To obtain good statistics and a precise measurement of the trap stiffness, Brownian motion must be recorded long enough.  $k_u$  is given with an accuracy of  $1/N$  if the fluctuations are analyzed over a period  $N^2$  times larger than  $1/f_c$ . In practice, we always adjust the measurement time for reaching errors lower than 10%, for example, a stiffness of  $10^{-7}$  N/m ( $1/(2\pi f_c) = 0.42$  s) is evaluated with a 16,384-frames acquisition at 25 Hz, (total time  $\Delta T = 655$  s), leading to an accuracy of  $\sqrt{1/(f_c \Delta T)} \sim 6.5\%$ .

In our experiment, as may be seen in Fig. 8, the spectra are indeed Lorentzian when the proportional feedback coefficient  $P_u$  is not too large. In this regime, the simplified model of the tweezers may be applied, and the measure of  $k_u$  using the equipartition theorem is valid (see Fig. 9). Nevertheless, as  $P_u$  is increased, this method does not remain valid anymore, and we can only use the low frequency asymptotic part of the spectrum to evaluate  $k_u$ . In fact, it appears clearly that the value of the low-frequency white noise scales with  $P_u^{-2}$ , whereas the cutoff frequency  $f_c$  increases linearly. As a consequence, when  $P_u$  increases, the trap characteristic time  $1/(2\pi f_c)$  decreases, and, above a critical value  $P_{uc}$ , it becomes significant compared with the delay in digital feedback (roughly two video frames). Resonance then occurs, leading to an instability that forbids higher feedback parameters and restrains the use of Eq. 10



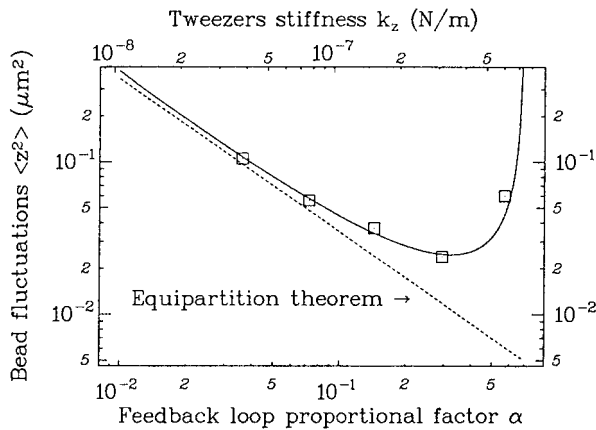


FIGURE 9 Mean square fluctuations versus the tweezers stiffness  $k_z$  (top axis) and the proportional feedback coefficient  $\alpha$  (Eq. 13, bottom axis). For ideal tweezers, the equipartition theorem applied to the simple model (Eqs. 8 and 10) gives a straight line (dashed line). For real tweezers, the mean square fluctuations calculated from the experimental spectra of Fig. 8 (squares) coincide with the prediction of the digital feedback model (solid line, calculated from Eq. 16 with  $L_0^2$  and  $\Delta$  as determined in Fig. 8). As the feedback proportional coefficient (i.e., the stiffness) is increased, the fluctuations decrease until they start to increase again because ringing occurs in the servo loop.

at small stiffness values (maximal trap stiffness of  $\sim 10^{-7}$  N/m).

### Effect of the digital feedback loop delay

To correctly describe the servo loop at high-feedback parameters, we must work with discrete times and recurrent relations. Let  $u_n$  be the position of the bead at image  $n$ , this parameter is driven by the equation,

$$u_{n+1} = u_n - \alpha u_{n-\Delta} + L_n, \quad (11)$$

where  $L_n$  is the displacement due to the Langevin force. As we can see, the bead position  $u_{n+1}$  at image  $n+1$  depends on its position at image  $n$  but also on its position at image  $n-\Delta$  through the feedback correction  $\alpha u_{n-\Delta}$ . Indeed, due to the delay  $\Delta$  between the video acquisition and the control of the magnetic field, the harmonic correction to the position at time  $n$  could only proceed using a previous particle location. Typically, the video camera has a delay of one image, and the acquisition hardware and software are responsible for the delay of an additional image, leading to  $\Delta \sim 2$ . Finally, during the time lapse  $\delta t$  of one image (40 ms here), the spring force  $k_u u_{n-\Delta}$  is balanced by the sole viscous drag, and, therefore, the equation of the dynamic leads to

$$k_u u_{n-\Delta} = \Gamma \eta r \cdot \frac{\alpha u_{n-\Delta}}{\delta t}, \quad (12)$$

i.e.

$$\alpha = \frac{k_u \delta t}{\Gamma \eta r} = \frac{A_u I_z P_u \delta t}{\Gamma \eta r} = 2\pi f_c \delta t. \quad (13)$$

It is convenient to consider Eq. 11 in Fourier space where the Brownian fluctuations of the Langevin force are

$$L_n = L_0 e^{2i\pi n} \quad \text{with} \quad L_0^2 = \frac{4k_B T \delta t^2}{\Gamma \eta r} = 4D \delta t^2. \quad (14)$$

Note that  $L_0^2$  is a noise density expressed in  $\mu\text{m}^2 \text{Hz}^{-1}$ . The bead displacement may then be written,

$$u_n = u(f) e^{i(2\pi n + \phi)}, \quad (15)$$

with an amplitude given by

$$|u(f)|^2 = \frac{L_0^2}{|e^{2i\pi f} - 1 + \alpha e^{-2i\pi f \Delta}|^2}. \quad (16)$$

This equation would be valid for a camera sampling the image for an infinitely small amount of time at each acquisition. Standard cameras integrate light over a significant fraction  $\delta t_i$  of the acquisition period  $\delta t$ . This averaging, together with the aliasing, introduces a filtering that slightly damps the signal at high frequency (Gittes and Schmidt, 1998). Consequently, we are obliged to introduce a correction  $\text{Cr}(f)$  in each data processing (see Appendix.).

Fitting Eq. 16 multiplied by  $\text{Cr}(f)$  to the experimental data, we obtain the values of the three parameters  $L_0^2$ ,  $\alpha$ , and  $\Delta$ . The fit is quite good and describes correctly the ringing behavior occurring when the proportional feedback  $P_u$  is large (Fig. 8). More precisely, at a given  $\Delta$ , it is the parameter  $\alpha$  that determines the system behavior: if it is too high, i.e., if  $f_c$  reaches one tenth of the sampling frequency (Eq. 13), the bead starts to oscillate (Fig. 9).

In summary, the stronger the feedback the higher the effective spring constant  $k_u$  is and the faster the bead reacts. However, the delay due to the video acquisition and treatment limits this feedback. Typically, the maximum frequency at which the feedback loop can safely operate is  $1/10$  of the acquisition frequency.

### Effect of the integral correction

The integral component  $K_u \Sigma(u)$  of the feedback loop allows, for instance, delivery of a constant current  $I_z$ , which levitates the bead even though the error signal in  $z$  is zero. Introducing the integral feedback requires modification of Eq. 11 as follows:

$$u_{n+1} = u_n - \alpha \left[ u_{n-\Delta} + \beta \sum_{i=-\infty}^{n-\Delta} u_i \right] + L_n, \quad (17)$$

with  $\beta = K_u/P_u$ . In Fourier space, this leads to

$$|u(f)|^2 = \frac{L_0^2}{\left| e^{2i\pi f} - 1 + \alpha e^{-2i\pi f \Delta} \left[ 1 - \frac{i\beta e^{i\pi f}}{2 \sin(\pi f)} \right] \right|^2}. \quad (18)$$

Again, this is the response using an ideal camera. With a real camera, we must correct this equation by  $Cr(f)$  (see Eq. 32). The coefficient  $\beta$  must be small because it introduces a phase shift. Proper values should be kept smaller than a tenth. In these conditions, the lowest frequencies of the bead fluctuations are strongly filtered out (see Fig. 12 A) and the stability of the system is improved.

When the integral feedback is used, the stiffness of the tweezers  $k_u$  depends on the frequency, and is thus not rigorously defined. However, we will still use  $k_u$  to characterize the stiffness; this effective  $k_u$  being the one measured if  $\beta$  is set to zero while all other parameters are kept constant.

### Calibration against the viscous drag

The numerical results obtained by the different calibration methods are discussed in Comparison of the Three Calibration Methods below. Viscous drag is often used to calibrate optical tweezers. In our case, it does not require mechanically moving any part of the setup. We simply rely on the software to change the virtual potential well position. A 4.5- $\mu\text{m}$  super-paramagnetic bead is locked in  $x$ ,  $y$ , and  $z$  at 10  $\mu\text{m}$  above the surface. We then move the set particle position in  $u$  by using a square wave signal, while we limit the maximum electromagnet current  $I_u$  to an absolute value  $I_{um}$  (Fig. 10 A). This threshold thereby defines the maximum bead velocity  $V_u$  in direction  $u$ . The object trajectory may be seen in Fig. 10 B, it is a slow rate-limited square wave that is repeated several times to allow averaging and then noise reduction. By varying  $I_{um}$ , we construct the calibration curve that relates the bead velocity to the driving current. As seen in Fig. 11,  $V_u$  and  $I_u$  are proportional, and we can thus define the measured proportionality constant,

$$B_u = V_u/I_u. \quad (19)$$

Because the force  $F_u$  acting on the bead is linked to its velocity by the Stokes' law,  $F_u = \Gamma \eta r \cdot V_u$ , it becomes proportional to the driving current  $I_u$  and, from Eq. 2, we have

$$A_u = B_u \cdot \Gamma \eta r. \quad (20)$$

The quantity  $\Gamma \eta r$  may be obtained either by optically measuring the bead radius and knowing the fluid viscosity or, in an absolute determination, by using the high-frequency bead fluctuations as described previously.

The calibration along  $z$  can be done by driving  $I_z$ . However, because the range of measurement in the vertical direction does not exceed 10  $\mu\text{m}$  (i.e., the size of the calibration image), special care must be taken to avoid losing the bead.

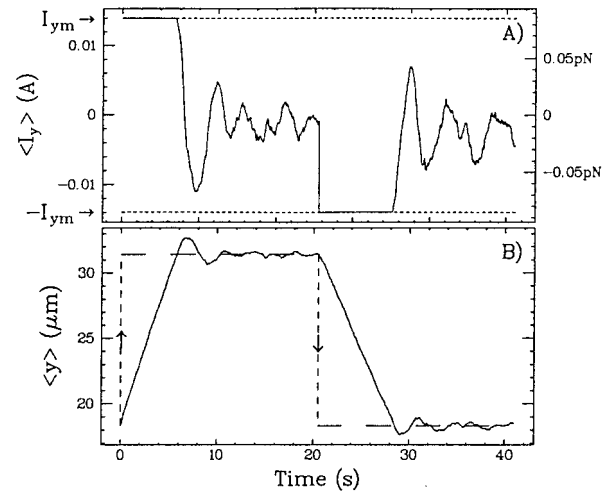


FIGURE 10 Procedure for tweezers calibration using Stokes' law. (A) Averaged coil-driving current producing the back and forth bead motion. (B) Corresponding averaged oscillations of the bead with constant moving velocity. The dash line corresponds to the imposed well position. When the calibration is achieved, the driving current may be converted in force as done on the right axis of panel A.

### Calibration using the Brownian fluctuations

When working with micrometric objects in fluids, Brownian fluctuations are important. Although they usually limit the accuracy of any measurement, they offer here two alternative calibration methods that are complementary to the previous one.

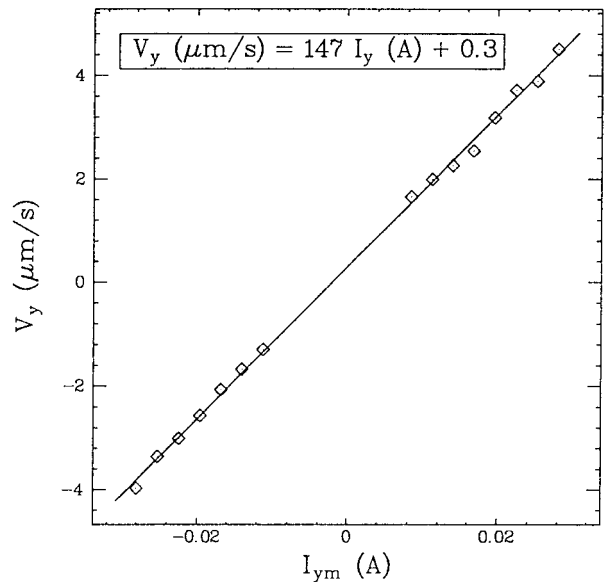


FIGURE 11 Calibration along  $y$  using Stokes' law. We have reported the bead velocity  $V_y$  versus  $I_{ym}$ , the maximum value allowed on the driving signal. Note that the linear behavior is even found for large modulation. Small driving currents are inaccessible because they prohibit normal operation of the feedback loop.

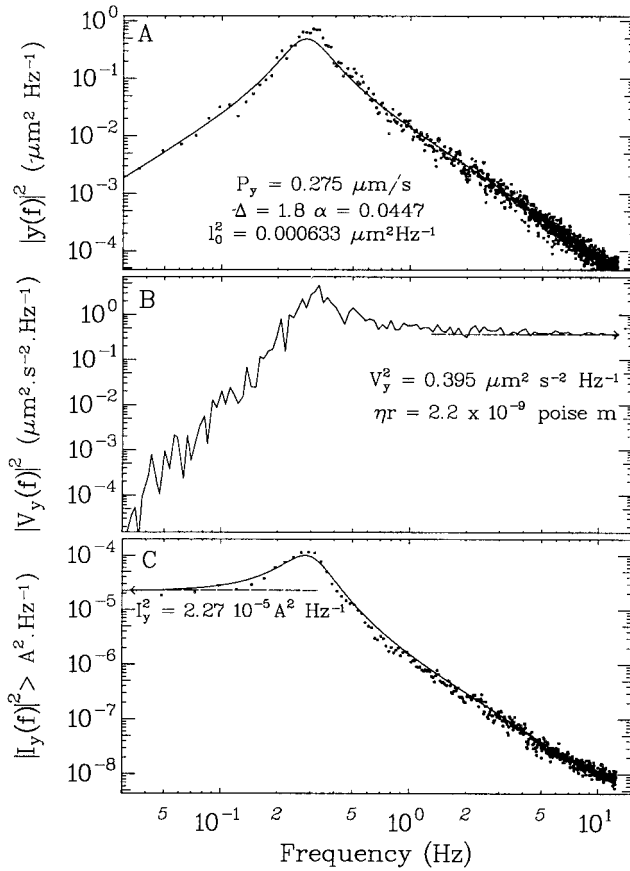


FIGURE 12 Calibration along  $y$  using the Brownian fluctuations of a trapped bead. (A) Experimental power spectrum of the  $y$  component of the bead fluctuations (dots) and fit to the feedback response defined by Eq. 18. (B) Power spectrum of the bead velocity fluctuations  $V_y$ . The high frequencies plateau at  $0.395 \mu\text{m}^2\text{Hz}^{-1}$  is related to  $\eta r$  via Eq. 9. (C) Power spectrum of the coil-driving current  $I_y$  in the same conditions (dots) and predicted current using the digital feedback model (solid line, calculated from Eqs. 1 and 18). The low-frequency asymptotic regime corresponds to the current required to compensate for the Langevin force.

The calibration procedure is completely achieved during particle locking by the magnetic tweezers. First, the computer records, simultaneously, the spontaneous fluctuations of the bead  $u(t)$  and the associated driving currents  $I_u(t)$ . In the absence of external perturbations, the trapped particle is stable in position because the feedback exactly compensates the Langevin random force at frequencies lower than the system characteristic cutoff frequency  $f_c$  (Fig. 12).

#### Asymptotic spectrum analysis

At low frequency, the feedback reaction equilibrates the Langevin force,  $F_u^2(f \ll f_c) = F_L^2$ . Thus we have, in  $x$  or  $y$ ,

$$A_u^2 I_0^2 (f \ll f_c) = 4k_B T \Gamma \eta r. \quad (21)$$

In  $z$ , for the linearized regime, where Eq. 5 holds, we have

$$4A_z^2 I_0^2 (f \ll f_c) = 4k_B T \Gamma \eta r. \quad (22)$$

As seen in Eq. 9, the high frequency bead velocity fluctuations  $V_u^2(f \gg f_c)$  can be used to calculate  $\Gamma \eta r$ . For  $u = x$  or  $y$ , we then obtain

$$A_u = \frac{4k_B T}{\sqrt{I_u^2(f \ll f_c) V_u^2(f \gg f_c)}}, \quad (23)$$

and, using Eq. 20,

$$B_u = \sqrt{\frac{V_u^2(f \gg f_c)}{I_u^2(f \ll f_c)}}. \quad (24)$$

Along the  $z$  direction, we have

$$A_z = \frac{4k_B T}{2I_0 \sqrt{I_z^2(f \ll f_c) V_z^2(f \gg f_c)}}. \quad (25)$$

and

$$B_z = \frac{1}{2I_0} \sqrt{\frac{V_z^2(f \gg f_c)}{I_z^2(f \ll f_c)}}. \quad (26)$$

#### Complete fit of the digital feedback response

As shown in Figs. 8 and 12, the entire power spectrum of the bead fluctuations may be fitted to the digital feedback response described by Eq. 18. This provides the values of the three relevant parameters  $L_0^2$ ,  $\alpha$ , and  $\Delta$ . Although  $\Delta$  is just the delay of the feedback and is of no direct use for the calibration, the values of  $\alpha$  and  $L_0^2$  allow us to extract the trap stiffness  $k_u$  and the viscous damping  $\Gamma \eta r$  (Eqs. 13 and 14).

$$\Gamma \eta r = \frac{4k_B T \delta t^2}{L_0^2} \quad \text{and} \quad k_u = \alpha \frac{4k_B T \delta t}{L_0^2}. \quad (27)$$

The current calibration is then obtained in  $x$  and  $y$ ,

$$A_u = \frac{4k_B T \alpha \delta t}{L_0^2 I_z P_u} \quad \text{and} \quad B_u = \frac{\alpha}{P_u \delta t I_z}, \quad (28)$$

and, in the  $z$  linearized regime (Eqs 6, 13, and 14),

$$A_z = \frac{4k_B T \alpha \delta t}{L_0^2 I_0^2 P_z} \quad \text{and} \quad B_z = \frac{\alpha}{P_z \delta t I_0^2}. \quad (29)$$

#### Comparison of the three calibration methods

Table 2 presents the numerical results obtained by applying the three calibration methods to the same bead (Figs. 8, 10, 11, and 12). Data along the  $y$  direction have been achieved with the three methods, but the viscous drag calibrations along  $x$  and  $z$  were not achieved on this particular particle and are then missing here.  $\Gamma_z$  is slightly larger than  $\Gamma_x$  and

**TABLE 2 Calibration parameters obtained by the three different methods\***

Calibration Parameter	Viscous Drag	Asymptotic Spectrum	Fitted Model	Units
$A_x$	—	$9.45 \pm 0.7$	$9.6 \pm 0.25$	pN/A
$A_y$	$6.1 \pm 0.2^\dagger$	$5.49 \pm 0.5$	$6.03 \pm 0.2$	pN/A
$A_z$	—	$176 \pm 10$	$200 \pm 5$	pN/A <sup>2</sup>
$B_x$	—	$227 \pm 15$	$241 \pm 5$	$\mu\text{ms}^{-1}\text{A}^{-1}$
$B_y$	$147 \pm 3$	$132 \pm 15$	$145 \pm 3$	$\mu\text{ms}^{-1}\text{A}^{-1}$
$B_z$	—	$3900 \pm 200$	$4560 \pm 80$	$\mu\text{ms}^{-1}\text{A}^{-2}$
$k_x$	—	7.28	$7.4 \pm 0.3$	$10^{-8}$ N/m
$k_y$	4.7	4.23	$4.64 \pm 0.2$	$10^{-8}$ N/m
$k_z$	—	15.1	$17.2 \pm 0.4$	$10^{-8}$ N/m
$k_x/P_x$	—	0.265	0.268	pN
$k_y/P_y$	0.1708	0.154	0.168	pN
$k_z/P_z$	—	0.138	0.157	pN
$\Gamma_x \eta r / 6\pi^\ddagger$	—	$2.2 \pm 0.06$	$2.12 \pm 0.04$	$10^{-9}$ poise·m
$\Gamma_y \eta r / 6\pi^\S$	—	$2.2 \pm 0.06$	$2.12 \pm 0.04$	$10^{-9}$ poise·m
$\Gamma_z \eta r / 6\pi$	—	$2.39 \pm 0.06$	$2.33 \pm 0.04$	$10^{-9}$ poise·m

The parameters  $A_z$  and  $B_z$  cannot be compared to their horizontal equivalent due to the nonlinear behavior of the force with  $I_z$ . A more reliable parameter is given by  $k_u/P_u$ , which is expressed in pN and compares the tweezers maximum force for the mean current  $I_0$ . Errors on fits were estimated by the boost-trap method.

\*All the results were obtained with  $\langle I_z \rangle = I_0 = 0.028$  A.

†Calculated using the  $\Gamma \eta r$  measured from the bead fluctuations.

‡Obtained from the calibration procedure along the  $x$  axis.

§Obtained from the calibration procedure along the  $y$  axis.

$\Gamma_y$  because the bead vertical motion is more affected by the horizontal boundary of the cell than the horizontal one (Happel and Brenner, 1991),

$$\Gamma_{x,y} = 6\pi \left(1 + \frac{9r}{16d}\right) \quad \text{and} \quad \Gamma_z = 6\pi \left(1 + \frac{8d}{9r}\right), \quad (30)$$

where  $d$  is the distance of the bead to the surface ( $10 \mu\text{m}$ ) and  $r$  the particle radius ( $2 \mu\text{m}$ ).

The three calibration techniques give very similar results and are somewhat complementary. The method relying on the asymptotic behavior of the position power spectrum just evaluates  $k_u$  and  $\Gamma \eta r$ , whereas the fit to the complete digital model depends also on  $\Delta$ , a third parameter not directly related to the calibration. Although this parameter can only be determined when ringing occurs (at large  $P_u$ ), the technique remains relatively simple because, for smaller  $P_u$ , the fit of the feedback loop response is not very sensitive to this  $\Delta$ . Finally, both of the above-discussed methods are well adapted to the linear regime of small forces and require only a few minutes signal recording. On the contrary, the viscous drag method is also appropriate for stronger forces and may even be applied in nonlinear regimes. The main drawback of this last technique is time consumption. It requires one signal recording for each point of the force velocity curve (Fig. 11).

## MICROMANIPULATION

### Translational movement

In the present setup, the gravity is the only way to drive the bead downward. As we have seen, the Langevin random

force may easily become larger than the weight of small particles, thus preventing the normal operation of the feedback loop. Consequently, in our experiment, we have used a bead with a diameter of  $4.5 \mu\text{m}$ . This object could easily be trapped and larger particles should also work well.

Figure 13 shows the successive center positions of a bead micromanipulated in the horizontal plane. The particle is locked in a virtual magnetic potential well, and this trap is displaced using manual keyboard commands. Note that the bead remains under the apparatus control as long as it is in the field of view of the camera. This property gives magnetic tweezers an obvious advantage over the optical ones, which lose particle control when it escapes from the potential well. For example, if a transient strong flow displaces the bead from the set position defined by the operator, the magnetic tweezers will bring it back to equilibrium point. In this situation, the bead moves with a maximum velocity determined by  $I_{um}$ , typically in the range of  $5\text{--}10 \mu\text{m/s}$ .

Magnetic particles can also be manipulated along the vertical, but, the calibration image being only  $10 \mu\text{m}$  high, special care must be taken not to lose the trapped object. Despite this, beads could be levitated up to  $50 \mu\text{m}$  above the surface while keeping the same trapping ability. This task seems difficult to achieve with usual optical tweezers relying on high numerical-aperture oil-immersion objectives (this is not true for a setup relying on water-immersion objective).

### Rotational movement

In Fig. 14, three beads are glued together by magnetic and adsorption forces, forming a linear triplet. The central one is

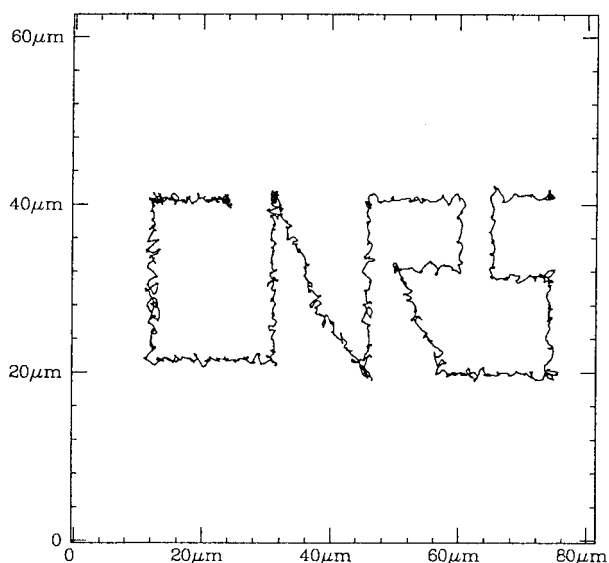


FIGURE 13 Control of the movement of a 4.5- $\mu\text{m}$  bead in solution. The position of the particle is controlled by the computer keyboard. The maximum displacement velocity is  $\sim 5 \mu\text{m/s}$ .

linked to the surface by a double-stranded DNA molecule, as in the previous force measurement experiment. While pulling this triplet with the classical currents configuration (Fig. 4 A), rotation is obtained by circular permutation of the currents applied to the electromagnets. Because the setup has a six-fold symmetry, the angular orientations that can be reached are necessarily multiples of  $60^\circ$  (the magnetic moment of the particle is always collinear with two opposite coils). At a rate of one permutation per field, the rotational speed can reach 10 turns per second.

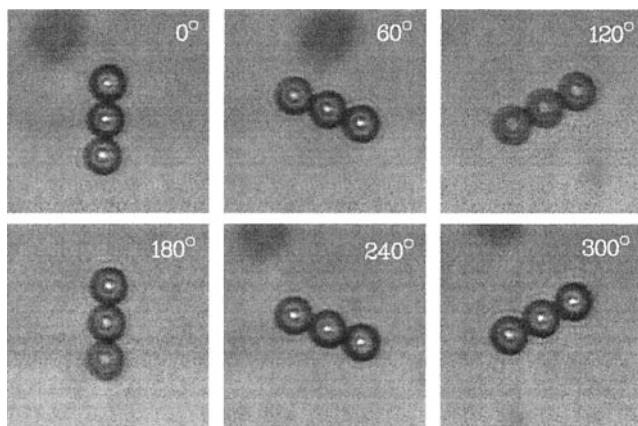


FIGURE 14 Counter-clockwise rotation of three aggregated beads linked to a surface by a double-stranded DNA molecule. This manipulation could also be done with a single locked particle, but we chose these images because of their higher visual impact.

## Performances and possible improvements

In feedback mode, the present setup, using a 4.5- $\mu\text{m}$  Dyna-bead is limited by the weight of the particle (0.16 pN in our precise example). If no other vertical force is applied, the vertical force compensating the bead weight fixes the driving current  $I_0$ . With this parameter set, the maximum horizontal forces reach 0.27 pN in  $x$  and 0.17 pN in  $y$  (the associated velocities are then, resp., 8 and 5  $\mu\text{m/s}$ ). Of course, once the bead has moved and attached to a substrate, stronger forces may be applied (up to 20 pN in  $z$  and  $\sim 5$  pN in  $x$  and  $y$ ).

Using the digital feedback model, it is easy to show that the tweezers stiffness equals

$$k_u = \frac{\alpha}{\delta t} \Gamma \eta r = \alpha f_s \Gamma \eta r. \quad (31)$$

For a given bead, the maximum stiffness value is obtained by setting the proportional feedback factor  $\alpha$  to the largest value. Nevertheless, this parameter is limited by the delay of the loop and by the acceptable level of ringing (typically  $\alpha = 0.3$ ). With 4.5- $\mu\text{m}$  beads, this leads to a maximum stiffness of  $\approx 0.3 \times 10^{-6}$  N/m, which corresponds to the value found experimentally in  $z$  (see the top axis of Fig. 9). Slightly smaller values are obtained in  $x$  and  $y$ , but all these limitations on  $\alpha$  are related to the two-frames delay in the acquisition. To further increase the stiffness, we should increase the sampling frequency  $f_s = 1/\delta t$  beyond the usual video rate.

The present apparatus was made for demonstrative purpose and its performances do not match those of cantilevers or optical tweezers. However, we think that these limitations are only of technical nature and could be solved easily in the future. For example, forces orthogonal to the optical axis are quite moderate (a few piconewton). Adding a symmetric set of electromagnets below the sample would improve the horizontal magnetic field gradients. Similarly, the magnetic trap is not as stiff as the optical one ( $10^{-7}$  N/m for the former compared to  $10^{-5}$  N/m for the latter). This is due to the low characteristic time scale ( $\sim 100$  ms) of any apparatus relying on video acquisition rate (25 Hz). New video cameras overcome this limitation, a factor 10 in the video rate can be easily achieved and would definitely improve both response time and stiffness of the magnetic tweezers.

Finally, our setup clearly demonstrates the ability to work with magnetic tweezers. They offer easy measurement of forces not easily accessible to optical tweezers (as weak as 0.05 pN) and rotation ability. In the future, we can imagine reproducing experiments such as single-molecular motor tracking (Yin et al., 1995). A kinesin-coated bead could be manipulated and brought into contact with a microtubule using the feedback system. When the motor would be attached to the microtubule, the tweezers could then be switched to a passive mode. The bead position could be

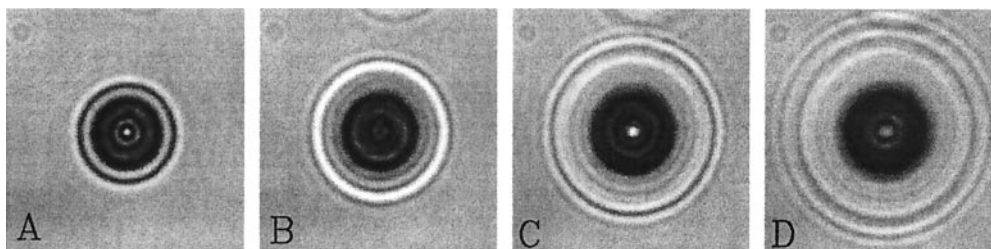


FIGURE 15 Images of a magnetic bead  $4.5 \mu\text{m}$  in diameter observed at various positions of the microscope focus plane: (A)  $z = 1 \mu\text{m}$ , (B)  $z = 3 \mu\text{m}$ , (C)  $z = 5 \mu\text{m}$ , and (D)  $z = 7 \mu\text{m}$ .

monitored with a nanometer resolution while the stretching force would be kept constant to a few piconewtons. An interesting feature of these tweezers is that the magnetic field direction can be adjusted, preventing bead rotation and, hopefully increasing the stiffness of the motor/bead complex. In the same fashion, DNA-stretching experiments (Strick et al., 1998), DNA polymerases (Maier et al., 2000; Wuite et al., 2000b), and topoisomerases analysis (Strick et al., 2000) could also be reproduced.

## CONCLUSION

Magnetic tweezers presented here meet all the requirements of micromanipulation and piconewton measurements on biological samples (Bensimon, 1996; Bustamante et al., 2000). We have first shown that it is possible to fully monitor the position of a micrometric magnetic bead immersed in an aqueous solution. This function is achieved by a set of electromagnets which, with the help of a 3D tracking system and a servo loop, traps the particle in a virtual potential well. Furthermore, we have demonstrated that our system is able to generate and measure forces in, roughly, any spatial direction. In this dynamometer mode, the tweezers can either be calibrated against the viscous drag or self-calibrated by analyzing the Brownian fluctuations of the trapped object. As an example of mechanical investigation on biopolymers, the elastic behavior of a single DNA molecule has been studied with stretching forces ranging from 50 fN to 20 pN.

In addition, magnetic tweezers are very efficient in spinning small-scale objects. Whereas optical tweezers required sophisticated and expensive hardware to produce torque (Sato et al., 1991; Friese et al., 1998; Paterson et al., 2001.), our simple apparatus can easily perform this task while rotating the direction of the magnetic field. Such ability had already been used for studying micromanipulated supercoiled DNA molecules (Strick et al., 1996) and their uncoiling by single topoisomerase (Strick et al., 2000). Because, like the  $F_1$ -ATPase (Noji et al., 1997), the flagellar motor (Ryu et al., 2000), and the RNA polymerase (Harada et al., 2001), an increasing number of proteins are found to

be involved in rotary motions, our tweezers should lead to numerous interesting applications in the field of single-molecule biomechanics.

The second advantage inherent to any magnetic handling device is its biocompatibility. Despite the use of infrared laser introduced by Ashkin and Dziedzic (1987), optical tweezers can still photodamage cells (Liu et al., 1996; Neuman et al., 1999) and proteins (Wuite et al., 2000a) within minutes, the process of such destruction remaining unclear. Wuite et al. proposed an integrated laser trap/flow control system where the limited use of the optical tweezers significantly increases the lifetime of the single enzyme under investigation (Wuite et al., 2000a). Magnetic tweezers could also appear as an alternative answer to laser-induced damage to biomaterial (within the intrinsic limitation that, contrary to optical tweezers, a micrometric particle should always be used as a handle or probe for studying cells and biomolecules).

## APPENDIX

### Positioning of the particle in the horizontal plane

To measure the  $x$  bead displacement  $\delta x$  that occurred since the last frame, the program analyzes a small image ( $128 \times 128$  pixels<sup>2</sup>) centered on the previous particle position. The  $x$  profiles of the object are averaged over typically 20 lines centered in the  $y$  direction. Assuming that the particle has a centro-symmetric image (Fig. 15), the averaged profile  $P(x + \delta x)$  should then be equal to  $P(-x - \delta x)$ . To determine  $\delta x$ , we just compute the correlation function  $C(\tau) = P(x) * P(-x + \tau)$ , which maximum occurs at  $\tau = 2\delta x$ . The correlation is obtained using a Fast Fourier Transform algorithm whereas the maximum position is computed by a polynomial interpolation. This procedure allows sub-pixel resolution, with an accuracy in the range of  $1/10$  to  $1/100$  of pixel (1 pixel corresponding to  $\sim 0.1 \mu\text{m}$ ). The spectral resolution is typically  $1 \text{ nm}/\text{Hz}^{1/2}$  for frequencies higher than 2 Hz (where the microscope drift can be neglected). Permutation of the  $x$  and  $y$  in the previous demonstration leads to the determination of the  $y$  movement.

### Positioning of the particle along the vertical axis

When the bead is slightly out of focus, this micrometric object appears surrounded by a series of concentric circles (Fig. 15 A–D). The tracking along the vertical  $z$  axis can use this characteristic pattern because the

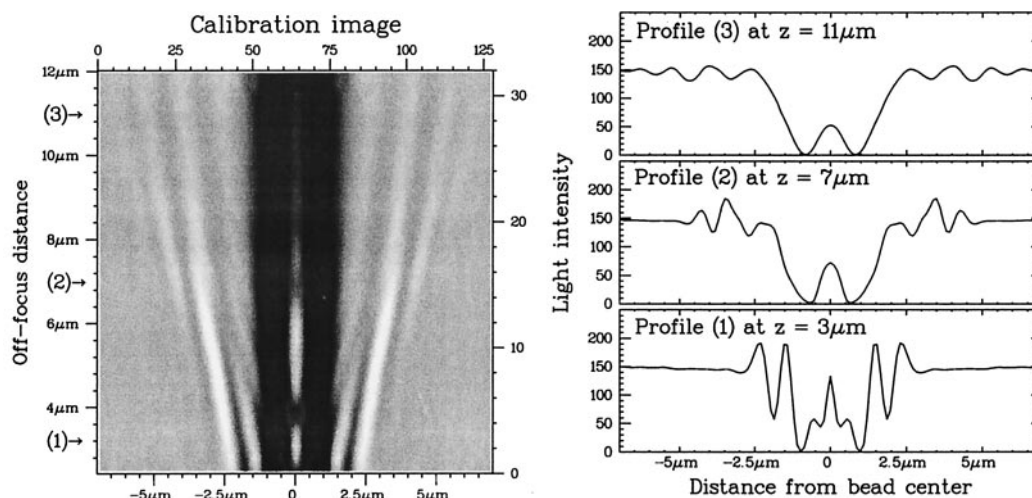


FIGURE 16 *Left.* Calibration image of a 4.5- $\mu\text{m}$  bead laying on the glass surface. Each line is obtained by measuring the radial profile of the object at a given  $z$  position of the microscope objective. *Right.* Intensity profile corresponding to 3, 7, and 11  $\mu\text{m}$ .

radius of the observed concentric circles depends on the position of the center of the bead relative to the focal plane of the objective. While tracking in  $x$ ,  $y$  a bead laid on the ground, we first build a calibration image. Typically, 32 radial profiles are recorded over a depth of  $\sim 10 \mu\text{m}$  above the particle center (Fig. 16). Then for vertical positioning, the radial profile of the object is compared in real time to this reference set. More precisely, a least-squares method enables a coarse determination of the nearest reference profiles. This process is then followed by an interpolation of the bead precise location. This interpolation relies upon the wave aspects of the diffraction rings. It turns out that the phase shift between successive profiles is fairly linear with their distance from the focal plane. Like for the  $x$ ,  $y$  tracking, resolution in the  $z$  tracking at high frequencies is in the range of  $1 \text{ nm/Hz}^{1/2}$ . Of course the vertical position of the bead can only be measured in a  $10\text{-}\mu\text{m}$  range above the focal plane. Further away, the oscillating rings progressively disappear.

### Camera correction in the Fourier space

All cameras integrate light during a fraction  $\delta t_i$  of the sampling period  $\delta t$  at which the video signal is produced. This integration over a rectangular time window leads to cardinal function in Fourier space. However, the integration occurs in two steps. Odd and even lines are recorded with a delay of  $\delta t$  leading to a cosine correction. Finally, aliasing of the signal always occurs because it is impossible to place a low-pass filter on each pixel. More details related to those problems may be found in Allemand (1997). The correction corresponding to our camera takes the form,

$$\begin{aligned} \text{Cr}(f) &= 2(1 - \cos(2\pi f/f_s))[\text{Cr}_0(f) + \text{Cr}_0(f_s - f) \\ &\quad + \text{Cr}_0(f_s + f) + \text{Cr}_0(2f_s - f)], \\ \text{Cr}_0(f) &= \frac{\sin(\pi\delta t_i(f/f_s)) \cos(\pi f/f_s)}{(\pi\delta t_i(f/f_s)) \cdot 4\pi(f/f_s)^2}. \end{aligned} \quad (\text{A1})$$

With  $\delta t_i = 0.97\delta t$ , we have  $\text{Cr}(0) = 1$ ,  $\text{Cr}(2\pi f_s/4) = 0.6772$ , and  $\text{Cr}(2\pi f_s/2) = 0.3475$ .

We thank Drs. J.-F. Allemand and T. Strick for helpful discussions and generous gift of DNA constructs, Drs. D. Bensimon and L. Jullien for constructive comments, Mrs. L. Brouard, J. Kerboriou, and J.-C. Sutra-

Fourcade for technical support, and Dr. N. Dekker for careful reading of the manuscript.

We acknowledge the support of the Centre National de la Recherche Scientifique, the Universit s Paris 6 and Paris 7, and the  cole Normale Sup rieure.

### REFERENCES

- Allemand, J.-F. 1997. *Micromanipulation d'une mol cule individuelle d'ADN*. PhD thesis, Universit  Pierre et Marie Curie Paris VI, France.
- Allemand, J.-F., D. Bensimon, R. Lavery, and V. Croquette. 1998. Stretched and overwound DNA form a Pauling-like structure with exposed bases. *Proc. Natl. Acad. Sci. U.S.A.* 95:14152–14157.
- Amblard, F., A. C. Maggs, B. Yurke, A. N. Pargellis, and S. Leibler. 1996a. Subdiffusion and anomalous local viscoelasticity in actin networks. *Phys. Rev. Lett.* 77:4470–4473.
- Amblard, F., B. Yurke, A. Pargellis, and S. Leibler. 1996b. A magnetic manipulator for studying local rheology and micromechanical properties of biological systems. *Rev. Sci. Instrum.* 67:1–10.
- Ashkin, A., and J. M. Dziedzic. 1987. Optical trapping and manipulation of viruses and bacteria. *Science*. 235:1517–1520.
- Bensimon, D. 1996. Force: a new structural control parameter? *Structure*. 4:885–889.
- Block, S. M., L. S. Golstein, and B. J. Schnapp. 1990. Bead movement by single kinesin molecules studied with optical tweezers. *Nature*. 348:348–352.
- Bouchiat, C., M. D. Wang, J.-F. Allemand, T. Strick, S. M. Block, and V. Croquette. 1999. Estimating the persistence length of a worm-like chain molecule from force-extension measurements. *Biophys. J.* 76:409–413.
- Bustamante, C., J. C. Macosko, and G. J. L. Wuite. 2000. Grabbing the cat by the tail: manipulating molecules one by one. *Nat. Rev. Mol. Cell Biol.* 1:130–136.
- Carrion-Vazquez, M., A. F. Oberhauser, S. B. Fowler, P. E. Marszalek, S. E. Broedel, J. Clarke, and J. M. Fernandez. 1999. Mechanical and chemical unfolding of a single protein: a comparison. *Proc. Natl. Acad. Sci. U.S.A.* 271:792–794.
- Cluzel, P., A. Lebrun, C. Heller, R. Lavery, J.-L. Viovy, D. Chatenay, and F. Caron. 1996. DNA: an extensible molecule. *Science*. 271:792–794.
- Crick, F. H. C., and A. F. W. Hughes. 1949. The physical properties of cytoplasm: a study by means of the magnetic particle method. *Exp. Cell Res.* 1:36–80.

- Evans, E., and K. Ritchie. 1997. Dynamic strength of molecular adhesion bonds. *Biophys. J.* 72:1541–1555.
- Finer, J. T., R. M. Simmons, and J. A. Spudich. 1994. Single myosin molecule mechanics: piconewtons and nanometre steps. *Nature.* 368:113–119.
- Florin, E.-L., V. T. Moy, and H. E. Gaub. 1994. Adhesion force between individual ligand–receptor pairs. *Science.* 264:415–417.
- Friese, M. E. J., T. A. Nieminen, N. R. Heckenberg, and H. Rubinsztein-Dunlop. 1998. Optical alignment and spinning of laser-trapped microscopic particles. *Nature.* 394:348–350.
- Gauthier-Manuel, B., and L. Garnier. 1997. Design for a 10 picometer magnetic actuator. *Rev. Sci. Instrum.*, 68:2486–2489.
- Gelles, J., B. Schnapp, and M. Sheetz. 1988. Tracking kinesin-driven movements with nanometre-scale precision. *Nature.* 331:450–453.
- Gittes, F., and C. F. Schimdt. 1998. Signals and noise in micromechanical measurements. *Methods Cell Biol.* 55:129–156.
- Guilford, W. H., R. C. Lantz, and R. W. Gore. 1995. Locomotive forces produced by single leukocytes *in vivo* and *in vitro*. *Am. J. Physiol. (Cell Physiol).* 268:C1308–C1312.
- Haber, C., and D. Witz. 2000. Magnetic tweezers for DNA micromanipulation. *Rev. Sci. Instr.* 71:4561–4569.
- Harada, Y., O. Ohara, A. Takatsuki, H. Itoh, N. Shimamoto, and K. Kinosita. 2001. Direct observation of DNA rotation during transcription by *Escherichia coli* RNA polymerase. *Nature.* 409:113–115.
- Happel, J., and H. Brenner. 1991. *Low Reynolds Number Hydrodynamics*. Kluwer Academics, Boston, MA.
- Heinrich, W., and R. E. Waugh. 1996. A piconewton force transducer and its application to the measurement of the bending stiffness of the phospholipid membranes. *Ann. Biomed. Eng.* 24:595–605.
- Ishijima, A., T. Doi, K. Sakurada, and T. Yanagida. 1991. Sub-piconewton force fluctuations of the actomyosin *in vitro*. *Nature.* 352:301–306.
- Kellermayer, M. S. Z., S. B. Smith, H. L. Granzier, and C. Bustamante. 1997. Folding-unfolding transitions in single titin molecules characterized with laser tweezers. *Science.* 276:1112–1116.
- Kishino, A., and T. Yanagida. 1988. Force measurement by micromanipulation of a single actin filament by glass needles. *Nature.* 334:74–76.
- Liu, Y., G. J. Sonek, M. W. Berns, and B. J. Tromberg. 1996. Physiological monitoring of optically trapped cells: effects of the confinement by 1064-nm laser tweezers using microfluorometry. *Biophys. J.* 71:2158–2167.
- Maier, B., D. Bensimon, and V. Croquette. 2000. Replication by a single DNA-polymerase of a stretched single strand DNA. *Proc. Natl. Acad. Sci. U.S.A.* 97:12002–12007.
- Merkel, R., P. Nassoy, A. Leung, K. Ritchie, and E. Evans. 1999. Energy landscapes of receptor–ligand bonds explored with dynamic force spectroscopy. *Nature.* 397:50–53.
- Moy, V. T., E.-L. Florin, and H. E. Gaub. 1994. Intermolecular forces and energies between ligands and receptors. *Science.* 266:257–259.
- Neuman, K. C., E. H. Chadd, G. F. Liou, K. Bergman, and S. M. Block. 1999. Characterization of photo-damage to *Escherichia coli* in optical traps. *Biophys. J.* 77:2856–2863.
- Noji, H., R. Yasuda, M. Yoshida, and K. Kinosita. 1997. Direct observation of the rotation of F<sub>1</sub>-ATPase. *Nature.* 386:299–302.
- Paterson, L., M. P. MacDonald, J. Arlt, W. Sibbett, P. E. Bryant, and K. Dholakia. 2001. Controlled rotation of optically trapped microscopic particles. *Science.* 292:912–914.
- Ryu, W. S., R. M. Berry, and H. C. Berg. 2000. Torque-generating units of the flagellar motor of *Escherichia coli* have a high duty ratio. *Nature.* 403:444–447.
- Sato, M., T. Z. Wong, D. T. Brown, and R. D. Allen. 1984. Rheological properties of living cytoplasm: a preliminary investigation of squid axoplasm (*Loligo peali*). *Cell Mobility.* 4:7–23.
- Sato, S., M. Ishigure, and H. Inaba. 1991. Optical trapping and rotational manipulation of microscopic particles and biological cells using higher-order mode Nd:Yag laser beams. *Electronics Lett.* 27:1831–1832.
- Schnitzer, M. J., and S. Block. 1997. Kinesin hydrolyses one ATP per 8-nm step. *Nature.* 388:386–390.
- Simmons, R. M., J. T. Finer, S. Chu, and J. A. Spudich. 1996. Quantitative measurements of force and displacement using an optical trap. *Biophys. J.* 70:1813–1822.
- Simson, D. A., F. Ziemann, M. Strigl, and R. Merkel. 1998. Micropipet-based pico force transducer: in depth analysis and experimental verification. *Biophys. J.* 74:2080–2088.
- Strick, T. R., J.-F. Allemand, D. Bensimon, A. Bensimon, and V. Croquette. 1996. The elasticity of a single supercoiled DNA molecule. *Science.* 271:1835–1837.
- Strick, T. R., J.-F. Allemand, D. Bensimon, and V. Croquette. 1998. The behavior of supercoiled DNA. *Biophys. J.* 74:2016–2028.
- Strick, T. R., V. Croquette, and D. Bensimon. 2000. Single-molecule analysis of DNA uncoiling by a type II topoisomerase. *Nature.* 404:901–904.
- Svoboda, K., and S. M. Block. 1994. Biological applications of optical forces. *Annu. Rev. Biophys. Biomol. Struct.* 23:247–285.
- Wang, N., J. P. Butler, and D. E. Ingber. 1993. Mechanotransduction across the cell surface and through the cytoskeleton. *Science.* 260:1124–1127.
- Wuite, G. J. L., R. J. Davenport, A. Rappaport, and C. Bustamante. 2000a. An integrated laser trap/flow control video microscope for the study of single biomolecules. *Biophys. J.* 79:1155–1167.
- Wuite, G. J., S. B. Smith, M. Young, D. Keller, and C. Bustamante. 2000b. Single-molecule studies of the effect of template tension on T7 DNA polymerase activity. *Nature.* 404:103–106.
- Yagi, K. 1960. The mechanical and colloidal properties of *amoeba* protoplasm and their relations to the mechanism of amoeboid movement. *Comp. Biochem. Physiol.* 3:73–91.
- Yin, H., M. P. Wang, K. Svoboda, R. Landick, S. M. Block, and J. Gelles. 1995. Transcription against an applied force. *Science.* 270:1653–1657.
- Zaner, K. S., and P. A. Valberg. 1989. Viscoelasticity of F-actin measured with magnetic microparticles. *J. Cell Biol.* 109:2233–2243.
- Ziemann, F., J. Rädler, and E. Sackmann. 1994. Local measurements of the viscoelastic moduli of entangled actin networks using an oscillating magnetic bead micro-rheometer. *Biophys. J.* 66:2210–2216.